

# Electric Cleanliness Algorithm based on Multi-Unit Interaction and Reallocation

NIKOLAOS E. FRAGIADAKIS, ANARGYROS T. BAKLEZOS,  
THEODOROS N. KAPETANAKIS, IOANNIS O. VARDIAMBASIS,  
CHRISTOS D. NIKOLOPOULOS

Laboratory of Telecommunications and Electromagnetic Applications,  
Department of Electronic Engineering,  
Hellenic Mediterranean University,  
Romanou 3, Chalepa, 73133, Chania, Crete,  
GREECE

*Abstract:* - Authors prior to this work proposed a methodology providing electric or magnetic cleanliness on spacecraft implementation by reordering equipment units. More precisely, since the mission's scientific goal relies on the payload's high sensitivity and accuracy for capturing the space environment, field minimization in measuring instrument location is imperative. Electromagnetic cleanliness is a constant open issue, since the mission target relies on clean measurements without including spacecraft self-emissions. A lot of science missions of ESA, NASA, or JAXA select usually a set of a couple of basic units as standard payload, i.e. batteries, Radio Frequency switches, Command units or Data Handling Management units, S-Band Transceivers, Power Distribution Units, etc. The later is usually measured and electromagnetically characterized by employing the on-ground facilities providing equivalent radiating models. This work provides a supplementary module to the formerly created framework for an entire unit positioning approach, taking into account the unit's test-level data, for suitable allocation of the space vessel's equipment toward electric cleanliness purposes taking into consideration the unit's induced behavior.

*Key-Words:* - Differential Evolution, Electric and Magnetic Cleanliness, Induced Dipole, Spacecraft Units Allocation, Inverse Electromagnetic Problems

Received: October 19, 2022. Revised: January 21, 2023. Accepted: February 24, 2023. Published: March 30, 2023.

## 1 Introduction

By definition, most space equipment consists of sophisticated systems and sensors that present tremendous sensitivity to electromagnetic interference (EMI), necessitating specific testing conditions and stringent cleanliness prerequisites [1], [2], [3]. To avoid EMI/EMC problems at the system level, assessment and analysis of the radiated fields, electric as well as magnetic, of the devices/harnesses on board a satellite, are required throughout the design phase, [4], [5], to make it possible for the on-site technical and scientific team to put together an arrangement of the platform units with field emissions at the various sensitive sensor sites in accordance with the specific mission requirements, the units are identified with regard to their electric and/ or magnetic emissions. Additionally, it is standard practice to model the aforementioned devices at the unit level as a means to get the ability to extrapolate all measured fields in the nominal position of the sensors for an initial

placement of each unit that represents the best engineering guess.

Naturally, this frequently results in emission fields that much exceed the needs of the technological and scientific objectives. The typical solution for these problems is the relocation of the units with considerable field emissions as far away from the chosen locations of the sensors, [6]. Given that there is a certain amount of platform space available, this solution has a limited range of applications. Booms were therefore used to introduce a further distance between the sensors and the rest of the platform, but as missions become more complicated and carry more units, the requirements also become more demanding.

For these kinds of problems, more sophisticated methods have been used, namely shielding in its passive form, [7], [8], of either custom sub-components, [7], or whole units of equipment, for example, reaction wheels, that commonly have emission problems. Metglass or Mu-metal, [6], [9] are often used materials that are suitable for this

operation. Shielding is a solution that unintentionally increases the platform's overall bulk and can only be used on a select few units in order to maintain operational efficiency.

To further reduce emissions, at the cost of complexity, a technique known as active mitigation which targets the cancelling out of the emitted fields, is used. This technique uses additional, carefully chosen, "artificial" sources placed precisely in the platform in order to generate the suitable opposing fields that abolish effectively either a selected unit's field, [7], [10], or the platform's entire field in chosen spots, regions or areas of interest, with the more sensitive equipment, devices, or sensors, [7], [10], [11]. This method includes low-frequency active systems, [10], [11], as well as DC issue remedies like compensatory magnets, [6], [7].

The frequency range at which the various mission-specific sensors operate is another crucial feature of the cleanliness topic that is highlighted by this frequency diversification. These mission's specific parameters define the cleanliness criteria, which consecutively determine the scope of the required unit characterization and the proper problem-solving techniques. Direct Current's (DC) issues are widely known and have to be prevented or limited from the mission's planning phase, [12], using the help of existing rules. Avoiding permanent magnets, and decreasing current loops' areas, [13], to back-wire solar panels, [14], are only some of the DC magnetic field's precautionary measures. The system's design is significantly influenced by the electrostatic problem. Furthermore, the differential electric potential of any two places on the space vessel's surface must be kept minimum, because surface charges change the platform's electrostatic environment (commonly below 1V). All of the spacecraft's surfaces must be highly conducting for this to occur, [15]. On the other hand, the cleaning difficulties of the Alternating Currents (AC) of low frequency are a relatively new area, that is drawing more and more focus, [9], [10], [11], [13].

As previously noted, any whole system-level EMC project must adhere to high magnetic and electric cleanliness standards, containing magnetic and electric fields originating from any harness, device, or equipment mounted on the mission's platform. In the present paper, we suggest a methodology for DC and low frequencies, which focuses on (without being limited to) the electric field, in a manner suitable for the minimization of the field, which is emitted at the location of the sensor, taking into account the induced fields. This is accomplished by shifting the onboard equipment's

position and orientation. The authors have previously addressed different problems with similar field reductions, [16], [17]. However, usually, in missions, the instruments measuring the fields are extremely sensitive. In these cases, an arrangement appropriate for the electric field's minimization at the desirable position of the electric sensor based solely on the unit models of the units might be quite different from the reality due to the effect of the induced dipoles on the other units. This work provides a methodology that also considers the induced behavior of the units and showcases that the environment is indeed very different so a solution neglecting the induced dipoles is not adequate. Works related to the description of the induced dipole participation in the total electric field can be found in [18], [19]. It should be emphasized that the suggested methodology ignores emissions from cables and harnesses and only considers emissions from individual units.

The prediction of the complete spacecraft's radiated emissions, starting from unit-level or component-level measurements (characterization), (i) streamlines the testing process, (ii) lowers the overall EMC campaign cost, and (iii) also offers a way to allocate the space platform's equipment as a means to accomplish the required magnetic and electric cleanliness at particular locations, [16], [17].

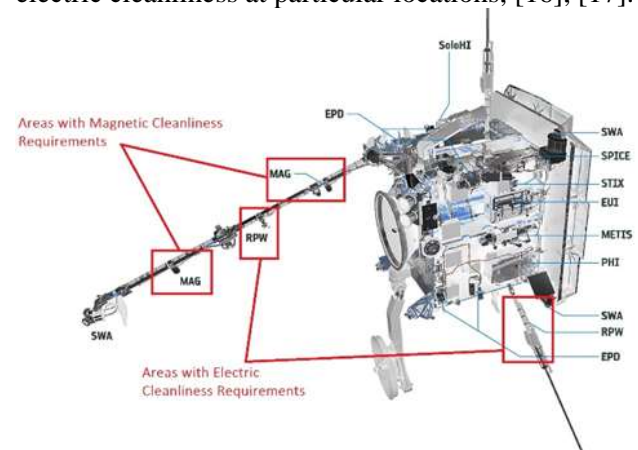


Fig. 1: Layout of sensor placement on the boom of Solar Orbiter signifying the areas with electric and magnetic cleanliness requirements. Credit: ESA.

## 2 Electric Field Equations & Problem Definition

The reduction of electric and/ or magnetic emissions at a site where multiple sensitive devices or sensors are intended to be installed is the essence of electromagnetic purity. Each unit's electromagnetic behavior is described and assigned to typical equivalent sources (such dipoles) as part of the unit-

level modeling process, which enables the identification of all units' field emissions throughout the space vessel for different operational routines. The vectorial summation of all the units' emissions, or at least those that have been shown to be significant contributions to the area of interest, is then used to estimate the system-level behavior. For the rest of the paper, the focus will be solely on the DC and low-frequency electric field.

## 2.1 Electric Field Formulation

In the current work, the frequency spectrum of interest ranges from 0 Hz to low frequencies below 300 kHz. The radiated fields from any source are thought to be quasistatic at these frequencies, especially near a source at distance considerably lower than one wavelength. Therefore the fields, electric and magnetic, are treated separately. The near-field approximation is appropriate for the particular circumstances of low frequencies and regions of interest in the vicinity of several unit sources. For any frequency of interest, another electric dipole serves as the primary representation for each unit's electric behavior in this work, which focuses on the electric field. The analysis presented completely supports a method with more dipoles per unit, but since this is not a frequent practice, it will not be expressly discussed in this study. In any instance, the moment and position variables inside the unit space are used to represent each such dipole for each frequency.

Denoting the vectors of a dipole source's position as  $\vec{R}_{dipole}$ , of the dipole's moment as  $\vec{p}$ , and of the  $m$  observation point's position as  $\vec{R}_m$ , and employing the near-field's approximation, we can express our electric field as:

$$E(\vec{n}, t) = Ae^{-i\omega t} \{3\vec{n}(\vec{n} \cdot \vec{p}) - \vec{p}\} \frac{1}{r^3} \quad (1)$$

Having in mind that  $\vec{p}$  denotes the moment vector of the dipole,  $r = |\vec{r}|$ ,  $\vec{r} = \vec{R}_m - \vec{R}_{dipole}$ , and  $\vec{n} = \vec{r}/r$ , the electric field  $\vec{E}$  at  $m$  with  $\vec{R}_m$  ( $x_m, y_m, z_m$ ) can be analyzed into its three components for every prominent emissions' frequency  $\omega_i = 2\pi f_i$ :

$$E_x = \frac{1}{4\pi\epsilon_0} \left[ \frac{3(x - x_m) \cdot C}{r^5} - \frac{p_x}{r^3} \right] \quad (2a)$$

$$E_y = \frac{1}{4\pi\epsilon_0} \left[ \frac{3(y - y_m) \cdot C}{r^5} - \frac{p_y}{r^3} \right] \quad (2b)$$

$$E_z = \frac{1}{4\pi\epsilon_0} \left[ \frac{3(z - z_m) \cdot C}{r^5} - \frac{p_z}{r^3} \right] \quad (2c)$$

where

$$C = (x - x_m) \cdot p_x + (y - y_m) \cdot p_y + (z - z_m) \cdot p_z$$

and

$$r = \sqrt{(x_m - x)^2 + (y_m - y)^2 + (z_m - z)^2}.$$

Consequently, the magnitude of a single dipole's total field for the frequency  $\omega_i$  is:

$$|E_{total}|_i = \sqrt{E_x^2 + E_y^2 + E_z^2} \quad (3)$$

When  $N$  number of units are considered to contribute to spacecraft's emissions, corresponding either to  $N$  distinct dipoles or to  $N$  ( $N > Q$ ) dipoles associated with only  $Q$  units (when some units correlate to more than one dipole), each  $s \equiv x, y, z$  component of the total electric field on the  $m$  evaluation spot is given by:

$$E_{Total\ s} = \sum_{i=1}^N \frac{A}{4\pi\epsilon_0} \left[ \frac{3(s_m - s_i) \cdot C}{r^5} - \frac{p_{si}}{r^3} \right] \quad (4)$$

resulting in a total electric field's magnitude:

$$|E_{total}|_N = \sqrt{E_{xTotal}^2 + E_{yTotal}^2 + E_{zTotal}^2} \quad (5)$$

## 2.2 Emissions on System Level Assembly

The dipole parameters have to be stated in the same coordinate system in order to complete the computations of (2) and the summations of (3) and (4). Commonly, this is chosen as the Spacecraft's Coordinate System (SCS), within which each unit, that describes the location of the various units in the spaceship's scheme, is capable of rotation around the three axes and movement in three dimensions, naturally within the limits of the spacecraft.

Taking into account the spacecraft origin SCS, the  $j$ th equipment unit's center (DUT's center) is assumed at  $(x_{oj}, y_{oj}, z_{oj})$ . All the characteristics are shown in Fig. 3, where each unit is assumed to be represented by  $k$  ( $k < i$ ) dipoles.

The transformation matrices shown in eq. (6) are used to calculate the positioning of the relevant electric moment's vector, when a DUT rotates in every possible direction (according to a respective orientation angle of the 3-axial SCS):

$$\left. \begin{aligned} R_x &= \begin{bmatrix} 1 & 0 & 0 \\ 0 & \cos\theta & -\sin\theta \\ 0 & \sin\theta & \cos\theta \end{bmatrix} \\ R_y &= \begin{bmatrix} \cos\omega & 0 & \sin\omega \\ 0 & 1 & 0 \\ -\sin\omega & 0 & \cos\omega \end{bmatrix} \\ R_z &= \begin{bmatrix} \cos\varphi & -\sin\varphi & 0 \\ \sin\varphi & \cos\varphi & 0 \\ 0 & 0 & 1 \end{bmatrix} \end{aligned} \right\} \quad (6)$$

resulting in the below effect on the spatial coordinates and moments:

$$\begin{pmatrix} x_{o_{kj}} \\ y_{o_{kj}} \\ z_{o_{kj}} \end{pmatrix}_{(rotated)} = R_z R_y R_x \begin{pmatrix} x_{o_{kj}} \\ y_{o_{kj}} \\ z_{o_{kj}} \end{pmatrix}_{(initial)} \quad (7)$$

$$\begin{pmatrix} p_{x_{kj}} \\ p_{y_{kj}} \\ p_{z_{kj}} \end{pmatrix}_{(rotated)} = R_z R_y R_x \begin{pmatrix} p_{x_{kj}} \\ p_{y_{kj}} \\ p_{z_{kj}} \end{pmatrix}_{(initial)} \quad (8)$$

The rotation sequence to the DUT's center follows a consistent pattern starting from the  $x$ -, continuing with the  $y$ -, and ending with the  $z$ -axis, using (7) and (8) to calculate the dipole source's coordinates and moment vectors.

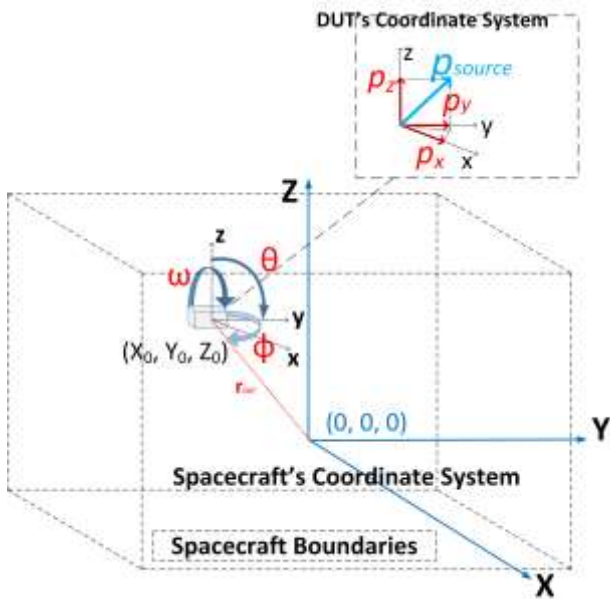


Fig. 2: Translation of DUT's electric moment vector from DCS to SCS.

The Device Coordinate System (DCS) coordinates of the  $k$ th dipole with respect to  $j$ th unit's origination are  $(x_{o_{kj}}, y_{o_{kj}}, z_{o_{kj}})$ . For computing the total electric field using (4) - (5), the  $(x_{o_{ij}}, y_{o_{ij}}, z_{o_{ij}})$  DCS coordinates must be translated to the corresponding SCS coordinates by:

$$\left. \begin{aligned} x_{o_{ij}} &= x_{o_{kj}} + x_{o_j} \\ y_{o_{ij}} &= y_{o_{kj}} + y_{o_j} \\ z_{o_{ij}} &= x_{o_{kj}} + z_{o_j} \end{aligned} \right\} \quad (9)$$

DUT's electric moment vector and orientation center are then stated in SCS for every potential rotation and/or displacement, using (7) and (9), respectively.

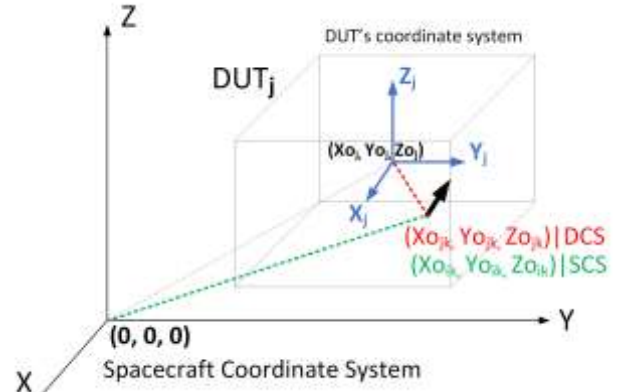


Fig. 3: Translation of DUT's center from DCS to SCS.

### 2.3 Problem Description and Definitions

Numerous DUTs are present on board every space mission and are bound by the spacecraft's hull. This has allowed us to replicate the spacecraft container with a cuboid volume that has dimensions of 2.5 m by 2.5 m by 3 m. (Fig. 2). The boundary area for the displacement of all the units is also included in this volume. To clarify, as stated in the Introduction, a number of real spacecraft devices (DUTs) of ESA's Earth Explorer "GOCE" mission are characterized and measured, [20], offering the base range from which the electric moments (and also the magnetic moments, if the same approach is followed) for this paper's artificial DUTs are drawn. These artificial DUTs are intended to highlight the practical features of this work.

In typical space missions, several different equipment units and instruments constitute the entire onboard real platform. The fusion of all the units and devices creates the precise and complete electromagnetic environment. However, only 3 or 4 of the devices often make a significant contribution, defining the behavior of the system's electromagnetic signature as a whole. Others are either mass-modeled with a predetermined moment value or deleted during the design phase, [21].

Table 1. Moments of the Electric Field for the 4 DUTs

DUT/Dipole	$p_x (fC \cdot m)$	$p_y (fC \cdot m)$	$p_z (fC \cdot m)$
1	-31	-38.5	-71
2	-42.7	26.6	17.7
3	-12.6	45.3	-94.1
4	10.1	-27.3	170

Table 2. Dipole's Coordinates in its Unit DCS

DUT/Dipole	$x (m)$	$y (m)$	$z (m)$
1	0.01	0	0
2	0	0.005	0
3	0	0	-0.03
4	0	0.01	0.01

Each of the four DUTs used in this study is modeled with one equivalent dipole given to it and is positioned in accordance with Table II. The four DUTs are thought to operate at a single similar frequency. Table I provides the associated electric moments for each DUT. The DUTs can be placed anywhere within the spacecraft's boundary constraints.

The aforementioned methodology can also be used when the DUT models include multiple electric (or with minor modifications, magnetic) dipoles, in order to take into consideration the induced electric moments, which can be modeled either typically also by additional dipoles, as demonstrated in this work, or precisely by more detailed representations, [3], [18], [19], [22], [23].

The position ( $\mathbf{OP}_e$ ), where electric and/or magnetic cleanliness needs to be attained, is where measuring probes or other victim devices exposed to space-vessel emissions need to be installed. In this study, the sensor volumes are shaped like cubes, each with a 0.2 m-long edge. The electric sensor's center is used for identification in the SCS ( $\mathbf{OP}_e = 3.318m, 0m, 0.75m$ ). To match various scenarios, the precise volume form of the observation site may be modified. The precise configuration is shown in Fig. 1. The allowable orientation of the DUTs in this work has a restriction. The DUTs must always sustain a face that is parallel to the space-vessel's base surface, which is necessary in order to mount the DUTs on the inside surfaces or walls of the spacecraft. The discretized numbers  $\{0^0, 90^0, 180^0, 270^0\}$  for the angles and are used to describe this constraint, and the units are only permitted to rotate about the z-axis (when  $0 \leq \varphi \leq 360$ ).

Assuming a specific set of DUTs, the orientation and positioning of artificial DUTs in relation to the sensor position can drastically alter the observed electric field there (modelled as electric moments). Equations (2) and (3) provide evidence for this. The positioning and orientation of the units at the sensor positions must be carefully chosen in order to reduce the electric field that they emit.

## 2.4. Unit-to-Unit Interaction

Since the frequency under investigation does not exceed a couple of hundred kilohertz, the scatterers near the remaining the  $N$  (in total) units of the spacecraft can be handled as oscillating dipoles, which are coherently provoked upon the scatterers by the incident fields, [18], [19]. These induced dipoles' calculations may be derived from boundary value problems, either quasi-static or even static. The medium around all scatterers have been modeled with  $\mu_r = \epsilon_r = 1$ . Moreover, due to the very long wavelength, the scatterer's dimensions may be considered excessively small, thus its precise shape and dimensions have no effect. Consequently, any scatterer may be handled as one sphere with small radius in the interior of a uniform total field  $\mathbf{E}_{inc}$  generated by the rest  $N-1$  components. On the basis of the above-mentioned procedure, the interaction among units depends on frequency and has to be addressed individually for every single frequency of concern  $f$ , in which, according to [24], [25], the material of the sphere-scatterer is affecting the induced electric dipoles' moments.

In the case of one perfectly conducting (PEC) sphere of small radius  $\alpha$ , the induced electric dipole's moment is:

$$\mathbf{p}_{ind}(f) = 4\pi\epsilon_o \alpha^3 \mathbf{E}_{inc}(f) \quad (10)$$

whilst, in the case of one dielectric sphere with a small radius  $\alpha$ ,  $\mu_r = 1$ , and isotropic, homogeneous, and frequency-dependent dielectric constant  $\epsilon_r(f)$  :

$$\mathbf{p}_{ind}(f) = 4\pi\epsilon_o \left( \frac{\epsilon_r(f) - 1}{\epsilon_r(f) + 2} \right) \alpha^3 \mathbf{E}_{inc}(f) \quad (11)$$

where  $\epsilon_o$  is the free-space dielectric permittivity.

For both events, we use as  $\alpha$  the radius of a sphere circumscribing the unit's volume  $L \times W \times H$  (given in  $m^3$ ):

$$\alpha = \frac{1}{2} \sqrt{L^2 + W^2 + H^2} \quad (12)$$

For example, a simple two-device interaction ( $N = 2$ ) is calculated in the following manner. We consider that unit 1 is the source (active) and in its neighbourhood unit, 2 is the victim (scatterer). Thus, when there is no electric field external to the unit pair  $\mathbf{E}_{ext}(f) = 0$ ,  $\mathbf{E}_{inc}(f)$  is the electric field caused by unit 1 at the position of unit 2 for the frequency  $f$ . Generally in the case of multiple units,  $\mathbf{E}_{inc}(f)$  has to be the vector summation of the electric fields generated from the rest of the units at the designated unit's position, assuming that each unit's AC electric behavior is expressed in its respective DCS for the  $f$  frequency, translated through coordinate rotations/translations to the SCS, characterized at the device level and modeled.

Then,  $\mathbf{E}_{inc_2}(f)$  in the scatterer's spot (using the  $\mathbf{E}_{inc_j}(f)$  notation) is only a straight computation of the electric field caused by the source dipoles  $d_{jk}$  ( $j$ th unit and  $k$ th dipole) as shown in Fig. 4 for a two-dipole ( $d_{11}, d_{21}$ ) easy case. Thereupon, examining a small conducting sphere's case, unit 2's provoked moment  $\mathbf{p}_{ind_2}(f)$  in the proximity of unit 1 is computed by (1).

The aforementioned provoked moment is coming from the dipole  $d_{ind_2}$  positioned at the unit-scatterer's center, following the  $d_{ind_j}(f)$  notation and describing unit 2's provoked behavior.

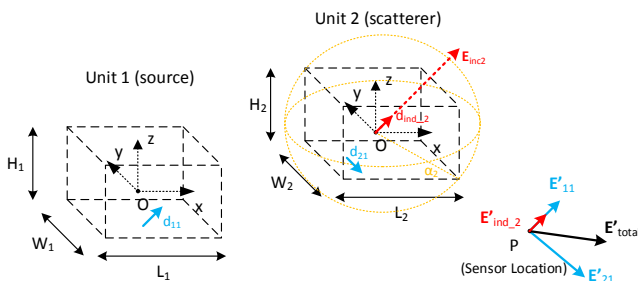


Fig. 4: Illustration of Unit 1's electric field effect on Unit 2 and the corresponding calculation of the total field on the sensor, ignoring induced field effects on Unit 1.

## 2.5 Description of the Field Minimization Heuristic Algorithm

The goal of this methodology is to offer a systematic method for creating an appropriate environment by jointly minimizing the electric field at a predefined volume, appropriately positioning and orienting the electric sources, and taking into account each unit's induced dipole under the influence (field) of the others. The coordinates of each cube center point identify the chosen volume (sensor) for the electric field.

In order to effectively cancel out their electric fields at the sensor's volume (centered at  $\mathbf{OP}_e$ ), the four units (the electric dipole sources of the DUTs) must be rearranged, and their orientation must be changed, according to the proposed stochastic method. This results in electromagnetic cleanliness. The well-known Differential Evolution (DE) computational optimization technique is used in this work to produce the answer, [26]. The set of 24 variables in total, corresponding to the 4 DUT centers' Cartesian SCS coordinates and rotation angles, is the answer. Figure 6 shows the proposed methodology's flowchart.

DE is used to computationally solve the minimization or maximization of a fitness/objective function. Generally, this function is expressing the rules regulating a prerequisite or an issue, through a mathematical formula for the process's desirable result. In this case, the best course of action would be to reduce the electric field  $|\mathbf{E}|_t$  at the relevant site ( $\mathbf{OP}_e$ ), so as

$$\mathbf{0} = |\mathbf{E}|_t \quad (13)$$

The minimization method starts by initializing the solution set, using the uniform distribution to choose at random out of the proper solution search space with 24 dimensions since each of the 4 DUTs of this work has 6 variables (3 center coordinates ( $x_i, y_i, z_i$ ) and 3 rotation angles ( $\theta, \varphi, \omega$ ) (with  $0 \leq \theta \leq 360^\circ$ ,  $\varphi \cong 0^\circ, 90^\circ, 180^\circ, 270^\circ$ , and  $\omega \cong 0^\circ, 90^\circ, 180^\circ, 270^\circ$ ). We will talk about the acceptable range for each DUT's center coordinates shortly. For the minimization of the goal function, the proposed algorithm is repeatedly seeking to improve any prospect solution by using the mutation, crossover, and selection operations (for the electric field at the sensor location).

Each prospect solution is generated, and then its viability is initially assessed in relation to DUT's impact. Note that, although the step is not included in the method's flowchart, we also perform this evaluation for the initial population's solutions (Fig. 4). Cuboid DUTs of dimensions  $a_i, b_i, c_i$  are expressed along by their circumscribed spheres to carry out the evaluations. The radius  $R_i$  of each sphere is given by

$$R_i = \sqrt{\left(\frac{a_i}{2}\right)^2 + \left(\frac{b_i}{2}\right)^2 + \left(\frac{c_i}{2}\right)^2} \quad (14)$$

To prevent overlap the two DUTs must follow the following rule

$$d \geq R_1 + R_2 \quad (15)$$

where  $d$  is the distance between DUT centers, while  $R_1$  and  $R_2$  are the corresponding circumscribed spheres' radii, shown in Fig. 5. The DUT's dimensions are presented in Table III.

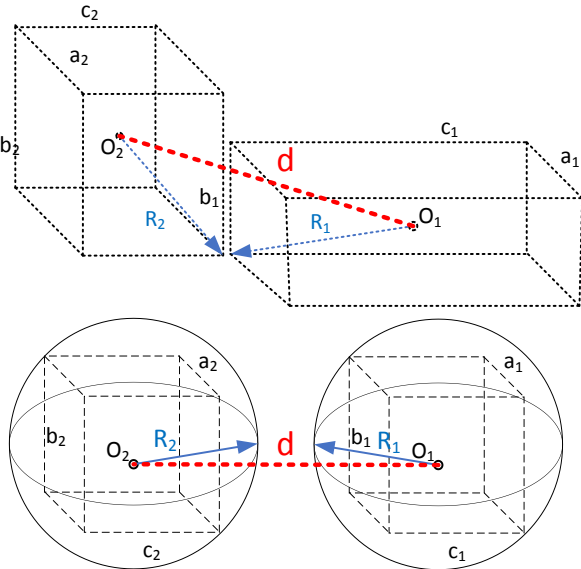


Fig. 5: Illustration of the overlap avoidance condition for the minimum distance of the DUTs centers placement.

Table 3. DUT's Dimensions

DUT	$L(m)$	$W(m)$	$H(m)$	$R_i(m)$
1	0.4	0.4	0.2	0.3
2	0.2	0.25	0.3	0.2194
3	0.4	0.1	0.1	0.2121
4	0.3	0.3	0.2	0.2345

If the unit overlap criterion is not satisfied, as shown in the algorithm's flowchart of Fig. 6, the candidate solution is deleted and substituted by a brand-new one. To further explore just physically possible options, this is done.

Each created prospect solution must also avoid setting the units outside of the spacecraft's perimeter. The DUT centers produced by the potential solution must be located more than  $R_i$  from the spacecraft boundary. The results of this constraint are the max/min values of the seeking area for the coordinates of the unit centers, which are listed in Table IV.

Since each variable of Table IV is unable to receive values beyond its permitted range, this requirement is evidently always satisfied. It is rather simple to impose additional regulations, such as

prohibited zones for particular units, precise relative orientations or lengths among particular unit couples or unit's boundary couples, etc. Such guidelines and statements are fully supported by the technique while formulating a particular issue.

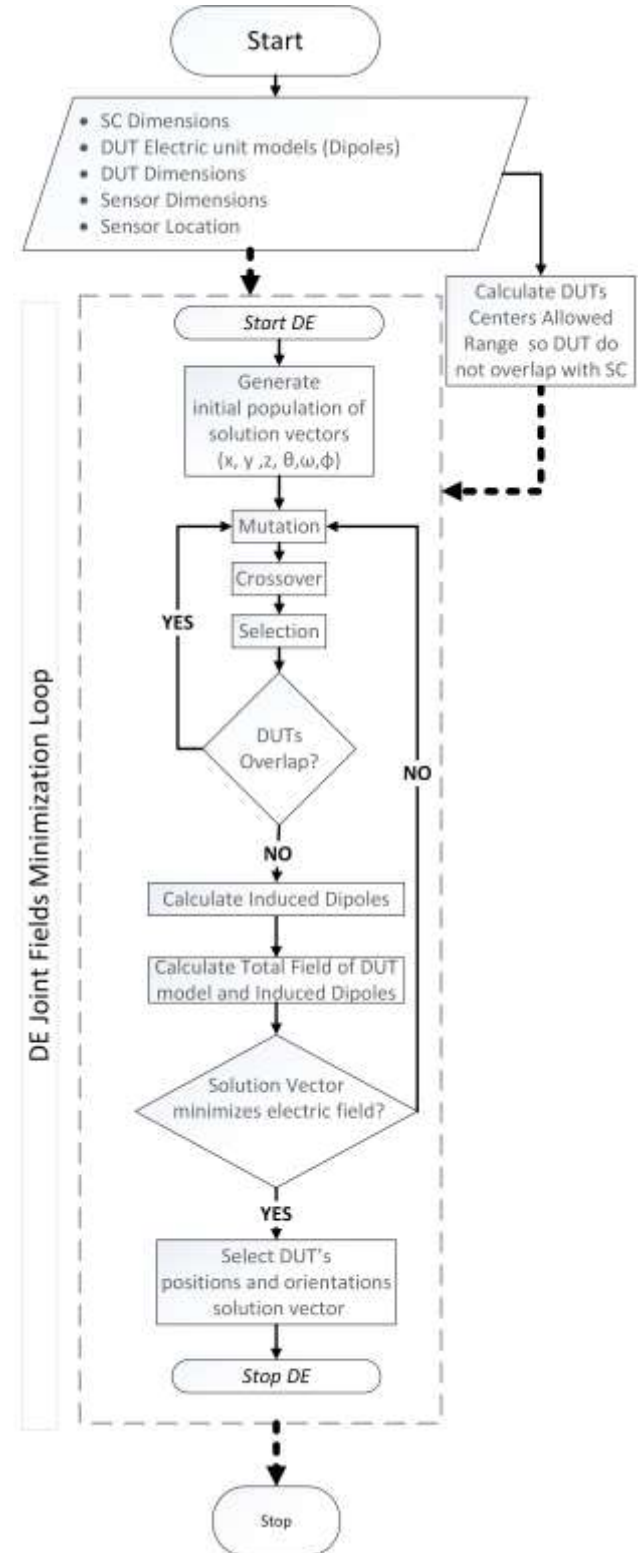


Fig. 6: Algorithm process in a flowchart.

The induced dipoles are calculated and added to the problem's dipole sources once each feasible solution has been developed. Calculating the total field at the sensor location entails iteratively determining the device combination that reduces this field value.

Table 4. Allowable Ranges of the Center Coordinates of the 4 DUTs

Variables	Min Allowable Values	Max Allowable Values
$x_1$	-0.95m	0.95m
$y_1$	-0.95m	0.95m
$z_1$	-1.2m	1.2m
$x_2$	-1.0306m	1.0306m
$y_2$	-1.0306m	1.0306m
$z_2$	-1.2806m	1.2806m
$x_3$	-1.0379m	1.0379m
$y_3$	-1.0379m	1.0379m
$z_3$	-1.2879m	1.2879m
$x_4$	-1.0155m	1.0155m
$y_4$	-1.0155m	1.0155m
$z_4$	-1.2655m	1.2655m

### 3 Discussion on Simulations

Before continuing with the results of the methodology, the importance of the inclusion of the induced fields to the problem is highlighted. The methodology was used to attempt to find a solution for the optimal placement of the four devices purposefully ignoring the induced dipoles. An assortment of units was found that (ignoring the induced dipoles) produced an electric field distribution, a  $yz$  cut of which is presented in Fig. 7. Obviously, the methodology managed to place the electric sensor (red box) in the minimum field location (deep blue area).

However, this result is erroneous since when actually including the induced dipoles in the calculation of the electric for that specific assortment of the units, it becomes apparent (Fig. 8) that the sensor (red box) is no longer in the minimum of the electric field. This result clearly showcases that the induced dipoles should always be included in the calculation in order to accurately predict the emitted field.

Correct algorithm execution results (including the induced dipoles) are presented in Fig. 9 and

recorded in Table V. The DUTs are obviously distinct from one another, and the particular combination of DUTs produces an electric field amplitude of  $5.43e-23$  (V/m) in the middle of the sensor volume. It should be noted for the extraction of the induced dipoles up to 10th order interactions was used with a field convergence limit equal to  $1e-30$ , [19]. Fig. 9 also depicts the boom (in blue highlight) and the electric sensor (in yellow highlight).

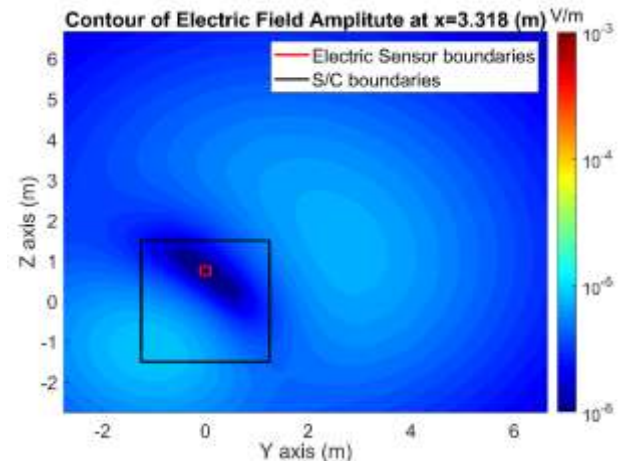


Fig. 7: E-field amplitude is calculated on the  $yz$  slice of space at  $(x = 3.318, y = 0, z = 0.75)$ , where the E-field sensor's center position is when optimized, without considering induced dipoles.

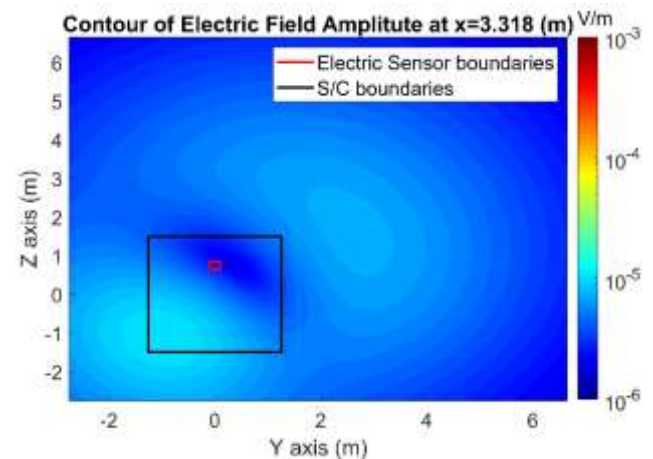


Fig. 8: E-field amplitude is calculated on the  $yz$  slice of space at  $(x = 3.318, y = 0, z = 0.75)$ , where the E-field sensor's center position is, taking into account induced dipoles.

Fig. 10, Fig. 11, and Fig. 12 show the magnitude contours of the electric field at the sensor's center, revealing that the algorithm successfully rearranges the various DUTs in order to place the electric sensor on the site with the least electric field at the  $xy$ ,  $xz$ , and  $yz$  planes, respectively. Figure 10 and

Figure 11 show three-dimensional electric field magnitude's cuts, that pass through the space vehicle and reveal high field's values because of the sources' close proximity to the spacecraft (DUTs). Therefore, it is typical to expect the sensor to be in a lower amplitude region. However, in the slices of Fig. 10 ( $xy$  plane near the sources), Fig. 11 ( $xz$  plane near the sources), and Fig. 12 ( $yz$  plane out of the sources) the sensor lies in the least field area. This is also demonstrated in Fig. 13, which shows how the electric field's amplitude varies with boom length (but is not limited to).

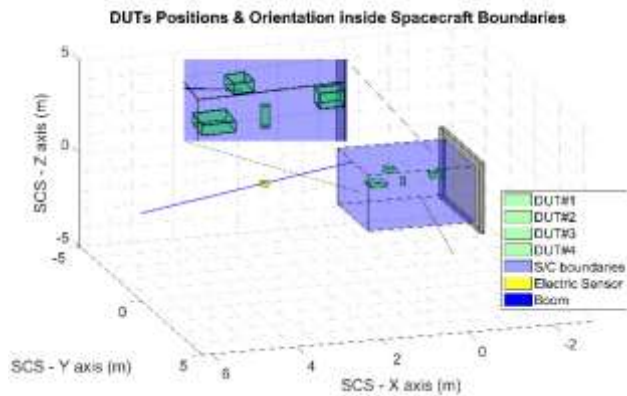


Fig. 9: The DUTs' placement inside the spacecraft, in compliance with the algorithm's solution to prevent overlap.

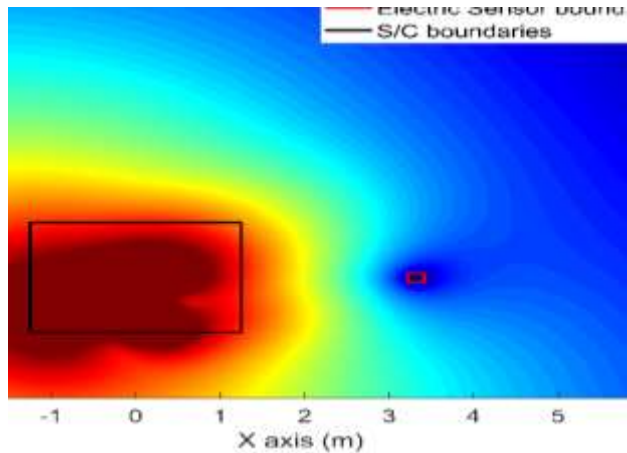


Fig. 10: E-field magnitude calculated on the  $xy$  slice of space at  $(x = 3.318, y = 0, z = 0.75)$ , where the E-field sensor's center position is.

The electric field's magnitude has its minimum upon the sensor's site, where it is reduced nearly 2 orders of magnitude in comparison to every other location along the boom, i.e. initiating from the spaceship's point  $(1.25m, 0m, 1.5m)$  with the attached boom and moving along the boom's line toward the sensor. The increased field's amplitude further along the boom shows emphatically how clean the sensor has become.

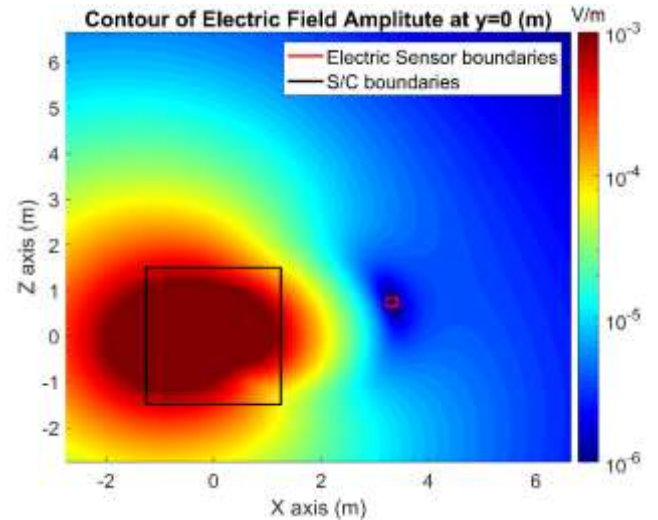


Fig. 11: The electric field magnitude calculated upon the  $xz$  slice of space at  $(x = 3.318, y = 0, z = 0.75)$ .

The boom line depicted in Fig. 13, being the blue line of Fig. 9, is totally residing on the  $xz$ -plane ( $y = 0$ ).

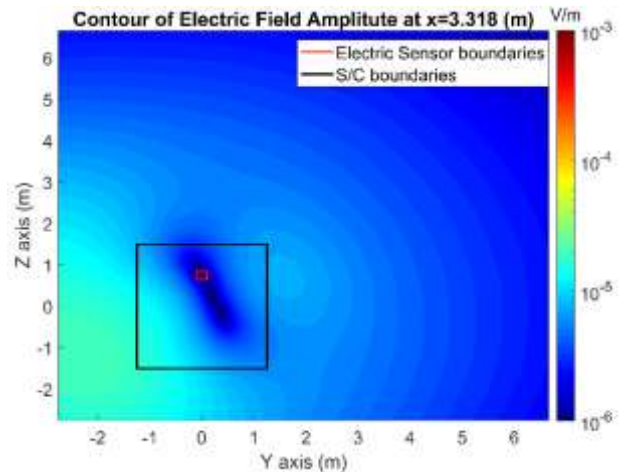


Fig. 12: The electric field magnitude calculated upon the  $yz$  slice of space at  $(x = 3.318, y = 0, z = 0.75)$ .

Table 5. Optimized Orientations and Center Positions of DUTs 1-4

DUT	$\theta^{(0)}$	$\varphi^{(0)}$	$\omega^{(0)}$	$x(m)$	$y(m)$	$z(m)$
1	0	0	0	0.4316	-0.9347	-0.3644
2	270	185.54	90	0.0994	-1.0306	0.2703
3	90	343.29	90	0.0549	-0.0971	0.1778
4	90	359	0	-0.9632	-0.9373	-0.1472

Figure 13 showcases the importance of adding the units' induced performance, as the minimization is not only substantially worst when an interaction

between units is not taken into consideration, but also the minimum has been moved to another location (at least 30 cm away).

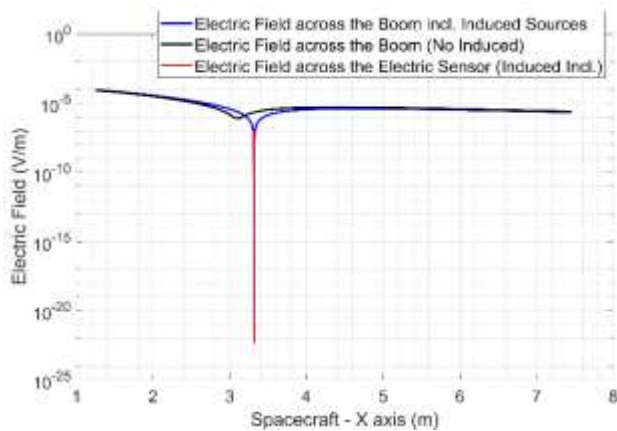


Fig. 13: Electric field's magnitude calculated across the boom's length, with the field minimum observed at the E-field sensor's position.

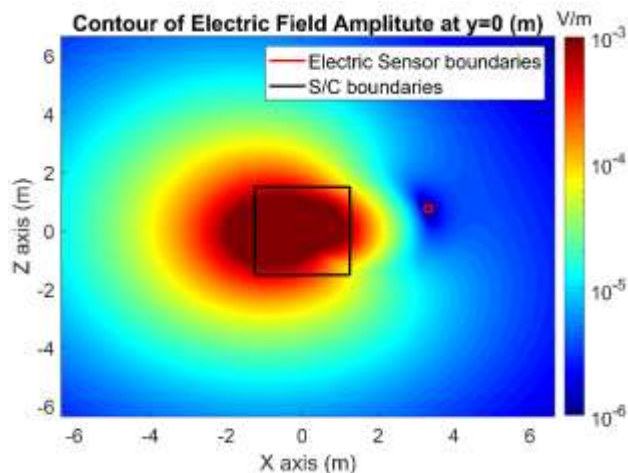


Fig. 14: Electric field's magnitude calculated upon the  $xz$  slice of space at  $(x = 3.318, y = 0, z = 0.75)$ .

The electric field's amplitude is estimated across the space vessel over a broader cubical region (approximately  $15 \times 15 \times 15 \text{ m}^3$ ), which further illustrates the electric field's reduction attained due to the herein outlined algorithm. The magnitude of the electric field in this region is shown in an  $xz$  plane cut in Fig. 14. It is clear that no other location in the study's area offers so a low-level field. This shows how our methodology can present unit layouts that achieve electric purity at levels sufficient for at least early mission design thoughts.

## 4 Conclusions

The methodology presented in the herein study uses heuristics to determine the best possible placement

of DUTs (regarding their orientation and exact position), when their electric moments are known and predefined at the unit-level measurement procedure within any spacecraft. This study's objective is the minimization of the total electric field's amplitude at chosen sensor positions while accounting for the units' induced performance. This work demonstrates (i) how the field could be decreased at several preselected locations of interest, and (ii) where the sensor needs to be positioned, given the electric and unit models. At the site of the sensor, the method is able to lower the field by around two orders. It is simple to implement limitations and restrictions on the placement of the units. Additionally, the concept is simple to combine with active strategies to improve the outcomes even more.

In the future, the process may be expanded to take into account cable emissions as well as harness ones, in order to produce harness paths that will satisfy both cleanliness goals. For results with significantly more accuracy and methodology with improved robustness, the algorithm has to additionally take into account the shielding effects of the spacecraft walls. This will make it possible to automatically provide a great beginning point for creating clean from electromagnetic fields platforms, using the proposed methodology. Additionally, the ultimate validation test should involve thorough system measurements and full use of the suggested methodologies in a real spaceship environment.

## References:

- [1] M. Pudney, S. King, T. Horbury, M. Maksimovic, C.J. Owen, and P. Laget, "Solar orbiter strategies for EMC control and verification," in *Proc. 2019 ESA Workshop on Aerospace EMC*, Budapest, Hungary, May 2019, pp. 1-6.
- [2] R.D. Leach and M.B. Alexander, "Failures and anomalies attributed to spacecraft charging," NASA Ref. Publ. 1375, 1995.
- [3] A. Junge and F. Marliani, "Prediction of DC magnetic fields for magnetic cleanliness on spacecraft," in *Proc. 2011 IEEE Int. Symp. Electromagnetic Compatibility*, Long Beach, USA, Aug. 2011, pp. 834-839.
- [4] F.S. de Adana, M.F. Catedra, J.M. Gomez, and R. Mittra, "Effective technique for system level prediction of the radiated emissions of electronic devices and cables inside satellites from unit level measurements," in *Proc. 2007 IEEE Int. Symp. Electromagnetic*

*Compatibility*, Honolulu, USA, July 2007, pp. 1-5.

- [5] F.S. de Adana, M.F. Catedra, J.M. Gomez, R. Mitra, J.B. Renuncio, F. Gutierrez, and M.A. Prieto, "An effective technique for system-level prediction of the radiated emissions of unknown sources inside low-Q cavities using unit-level measurements," *IEEE Trans. Electromagnetic Compatibility*, vol. 51, no. 2, pp. 181-191, May 2009.
- [6] M. de Soria-Santacruz, M. Soriano, O. Quintero, F. Wong, S. Hart, M. Kokorowski, B. Bone, B. Solish, D. Trofimov, E. Bradford, C. Raymond, P. Narvaez, C. Keys, P. Lord, J. Ream, R. Oran, B.P. Weiss, C. Russell, K. Ascrizzi, and L. Elkins-Tanton. "An approach to magnetic cleanliness for the Psyche mission," in *Proc. 2020 IEEE Aerospace Conference*, Big Sky, USA, Mar. 2020, pp. 1-15.
- [7] M. Boghosian, P. Narvaez, and R. Herman, "Magnetic testing, and modeling, simulation and analysis for space applications," in *Proc. 2013 IEEE Int. Symp. Electromagnetic Compatibility*, Denver, USA, Aug. 2013, pp. 265-270.
- [8] M. Pudney, S. King, C. Trenkel, F. Liebold, S. Strandmoe, P. Meyer, and M. Ehinger, "Advances in reaction wheel design for magnetic cleanliness," in *Proc. 2019 ESA Workshop Aerospace EMC*, Budapest, Hungary, May 2019, pp. 1-6.
- [9] K. Dang, P. Narvaez, J. Berman, K. Pham, and A. Curiel, "Magnetic shielding concepts for reaction wheel assembly on NASA Europa clipper spacecraft," in *Proc. 2020 IEEE Int. Symp. Electromagnetic Compatibility and Signal/Power Integrity (EMCSI 2020)*, Reno, USA, Aug. 2020, pp. 305-311.
- [10] A. Nicolai, S. Stoltz, O. Hillenmaier, J. Ludwig, C. Strauch, D. Grivon, L. Rossini, E. Onillon, T. Hellwig, and S. Scheiding, "Towards a magnetically clean reaction wheel with active magnetic field mitigation," in *Proc. 2019 ESA Workshop on Aerospace EMC*, Budapest, Hungary, May 2019, pp. 1-6.
- [11] A. Nicolai, S. Stoltz, L. Hafemeister, S. Scheiding, O. Hillenmaier, and C. Strauch, "The magnetically clean reaction wheel: Results and performance," in *Proc. 2022 ESA Workshop on Aerospace EMC*, May 2022, pp. 1-7.
- [12] A. Lassakeur and C. Underwood, "Magnetic cleanliness program on cubesats for improved attitude stability," in *Proc. 9th Int. Conf. Recent Advances in Space Technologies (RAST 2019)*, Instabul, Turkey, June 2019, pp. 123-129.
- [13] R. Kallenbach, T. Behnke, S. Engelke, K. Bubeck, and R. Henkelmann, "AC and transient magnetic emissions of the Juice Ganymede laser altimeter," in *Proc. 2022 ESA Workshop Aerospace EMC*, May 2022, pp. 1-6.
- [14] T.G. Stern and S. DeLapp, "Techniques for magnetic cleanliness on spacecraft solar arrays," in *Collection of Technical Papers - 2nd International Energy Conversion Engineering Conf.*, 2004.
- [15] V.A. Davis, M.J. Mandell, N.R. Baker, M. Brown-Hayes, G.T. Davis, R.H. Maurer, and C. Herrmann, "Surface-charging analysis of the radiation belt storm probe and magnetospheric multi scale spacecraft," *IEEE Trans. Plasma Science*, vol. 40, no. 2, pp. 262-273, Feb. 2012.
- [16] G.I. Koutantos, C.D. Nikolopoulos, A.T. Baklezos, and C.N. Capsalis, "Proper equipment ordinance for achieving EM cleanliness in space missions: The case of ELF electric sources," *IEEE Trans. Electromagnetic Compatibility*, vol. 62, no. 5, pp. 1686-1692, Oct. 2020.
- [17] C.D. Nikolopoulos, A.T. Baklezos, and C.N. Capsalis, "On achieving spacecraft level magnetic cleanliness with proper equipment ordinance of DC and ELF magnetic sources," *IEEE Trans. Electromagnetic Compatibility*, vol. 62, no. 6, pp. 2714-2724, Dec. 2020.
- [18] A.T. Baklezos, C.D. Nikolopoulos, P.K. Papastamatis, T.N. Kapetanakis, I.O. Vardiambasis, and C.N. Capsalis, "Early considerations for unit's induced electric behaviour characterization in the extreme low frequency domain," in *Proc. 2022 Int. Symp. Electromagnetic Compatibility (EMC Europe 2022)*, Gothenburg, Sweden, Sep. 2022, pp. 744-747.
- [19] A.T. Baklezos, C.D. Nikolopoulos, S.T. Spantideas, A.E. Giannopoulos, and C.N. Capsalis, "On the unit-to-unit interaction for electric field estimation up to the low frequency band," in *Proc. 2022 ESA Workshop Aerospace EMC*, May 2022, pp. 1-4.
- [20] A.T. Baklezos, C.D. Nikolopoulos, S.T. Spantideas, E.G. Chatzineofytou, M. Nicoletto, I. Marziali, D. Boschetti, and C.N. Capsalis, "Steady state emissions modeling of low frequency magnetic and electric fields generated by GOCE CDMU," in *Proc. 2019 ESA Workshop Aerospace EMC*, Budapest, Hungary, May 2019, pp. 1-5.

- [21] H.H. Park, H. Jin, T.Y. Kim, K.H. Kim, H.J. Lee, J.H. Shin, Y.H. Jang, and W.H. Jo, "Analysis of the KPLO magnetic cleanliness for the KMAG instrument," *Advances in Space Research*, vol. 69, no. 2, Jan. 2022.
- [22] A.S.K. Habila and W.H. Steyn, "In-orbit estimation of the slow varying residual magnetic moment and magnetic moment induced by the solar cells on CubeSat satellites," in *Proc. 2020 Int. Conf. Computer, Control, Electrical and Electronics Engineering (ICCCEE 2020)*, Khartoum, Sudan, Feb. 2021, pp. 1-6.
- [23] M.A. Pudney, G. Kapfunde, and L. Trougnou, "Induced magnetic field due to reaction wheel shielding," in *Proc. 2016 ESA Workshop Aerospace EMC*, Valencia, Spain, May 2016, pp. 1-6.
- [24] C.S. Obiekezie, D.W.P. Thomas, A. Nothofer, S. Greedy, L.R. Arnaut, and P. Sewell, "Complex locations of equivalent dipoles for improved characterization of radiated emissions," *IEEE Trans. Electromagnetic Compatibility*, vol. 56, no. 5, pp. 1087-1094, Oct. 2014.
- [25] C.D. Nikolopoulos, "Extremely low frequency electric field emissions for space applications: Measuring and modeling techniques," in *Electromagnetic Compatibility for Space Systems Design*. Hershey, USA: IGI Global, 2018, ch. 1, pp. 1-37.
- [26] R. Storn and K. Price, "Differential evolution - A simple and efficient heuristic for global optimization over continuous spaces," *Journal of Global Optimization*, vol. 11, pp. 341-359, Dec. 1997.

### **Contribution of Individual Authors to the Creation of a Scientific Article (Ghostwriting Policy)**

-Nikolaos Fragiadakis carried out part of the paper's conceptualization, methodology, software, validation, investigation, data curation, and writing—original draft preparation.

-Anargyros Baklezos carried out part of the paper's conceptualization, methodology, software, validation, investigation, resources, data curation, writing—original draft preparation, and writing—review, and editing.

-Theodoros Kapetanakis carried out part of the paper's software, validation, investigation, and data curation.

-Ioannis Vardiambasis carried out part of the paper's conceptualization, methodology, investigation, resources, writing—original draft preparation, writing—review and editing, supervision, and project administration.

-Christos Nikolopoulos carried out part of the paper's conceptualization, methodology, software, validation, investigation, resources, data curation, writing—original draft preparation, writing—review and editing, supervision, and project administration.

### **Sources of Funding for Research Presented in a Scientific Article or Scientific Article Itself**

This research received no external funding.

### **Conflict of Interest**

The authors have no conflict of interest to declare that is relevant to the content of this article.

### **Creative Commons Attribution License 4.0 (Attribution 4.0 International, CC BY 4.0)**

This article is published under the terms of the Creative Commons Attribution License 4.0

[https://creativecommons.org/licenses/by/4.0/deed.en\\_US](https://creativecommons.org/licenses/by/4.0/deed.en_US)